

1 Microsnoop: A Generalized Tool for Unbiased Representation of 2 Diverse Microscopy Images

3 Authors

4 Dejin Xun¹, Rui Wang^{2*}, Xingcai Zhang^{3*}, Yi Wang^{1,4,5*}

5 Affiliations

7 1. Pharmaceutical Informatics Institute, College of Pharmaceutical Sciences, Zhejiang
8 University, Hangzhou, Zhejiang 310058, China

9 2. State Key Lab of CAD&CG, Zhejiang University, Hangzhou, Zhejiang 310058, China

10 3. John A. Paulson School of Engineering and Applied Sciences, Harvard University,
11 Cambridge, MA 02138, USA

12 4. Innovation Institute for Artificial Intelligence in Medicine of Zhejiang University,
13 Hangzhou, Zhejiang 310018, China

14 5. State Key Laboratory of Component-based Chinese Medicine, Tianjin University of
15 Traditional Chinese Medicine, Tianjin 300193, China

16 *Corresponding author. Email: zjuwangyi@zju.edu.cn (Y.W.); xingcai@mit.edu (X.C.Z.);
17 ruiwang@zju.edu.cn (R.W.)

19 Abstract

20 Microscopy image profiling is becoming increasingly important in biological research.
21 Microsnoop is a new deep learning-based representation tool that has been trained on large-scale
22 microscopy images using masked self-supervised learning, eliminating the need for manual
23 annotation. Microsnoop can unbiasedly profile a wide range of complex and heterogeneous images,
24 including single-cell, fully imaged, and batch-experiment data. Its performance was evaluated on
25 seven high-quality datasets, containing over 358,000 images and 1,270,000 single cells with
26 varying resolutions and channels from cellular organelles to tissues. The results show that
27 Microsnoop outperforms previous generalist and even custom algorithms, demonstrating its
28 robustness and state-of-the-art performance in all biological applications. Furthermore, Microsnoop
29 can contribute to multi-modal studies and is highly inclusive of GPU and CPU capabilities. It can
30 be easily and freely deployed on local or cloud computing platforms.

31 MAIN TEXT

34 Introduction

35 Automatic quantitative profiling of microscopy images has become increasingly ubiquitous in
36 a broad range of biological research, spanning from small-scale investigations to high throughput
37 experiments¹. The analysis of visual phenotypes, which involves profiling intricate information
38 from images, has demonstrated its usefulness in diverse areas of biology². These include protein
39 localization³, cell cycle stage classification⁴, mechanisms of action predictions⁵, and high-content
40 drug discovery⁶. Additionally, the emergence of spatial omics has given rise to new requirements
41 for the quantification of microscopy images. For example, spatial proteomics methods can image
42 more than 50 disease-related proteins in a single tissue slice⁷, while spatial transcriptomics allows
43 for the simultaneous acquisition of both image data and transcriptional profiles⁸. These
44 developments underscore the need for a high-performance, generalist representation tool that can
45 effectively handle heterogeneous microscopy images.

46 The traditional approach to profiling microscopy images involves extracting predefined
47 morphological features, such as intensity, shape, texture, granularity, and colocalization⁹⁻¹⁰.
48 However, this method has several limitations, including low computational efficiency, potential
49 information loss, and sensitivity to image quality¹¹. To overcome these deficiencies, recent
50 advancements in computer vision and deep learning have given rise to learning-based feature
51 extraction methods that use representation learning. This technique involves pre-training a model
52 on pretext tasks and then using part of the network as a feature extractor for downstream analysis.
53 These methods can be divided into two categories: task-oriented custom methods and generalist
54 methods. Task-oriented methods^{4, 12-15} are pre-trained on data from the same source and designed
55 specifically for biological research, such as cell cycle stage prediction. In contrast, generalist
56 methods require training data that are not specific to any particular biological problem. One of the
57 most widely used generalist methods involves using models trained for ImageNet¹⁶ (a natural image
58 classification task), which has also been utilized in recent multi-modal research¹⁷.

59 However, the extent to which the feature extraction patterns learned from natural images can
60 capture the subtle phenotypes of microscopy images has not been fully validated by comparative
61 research. To better match the feature domain to downstream microscopy image profiling tasks, the
62 CytolmageNet¹⁸ study was conducted, where image representation was learned based on a
63 microscopy image classification task (890K images, 894 classes). Although this study demonstrated
64 comparable performance to ImageNet, it still relied on the supervised learning approach that can
65 be labor-intensive, prone to biases from semantic annotations, and potentially increase the difficulty
66 of achieving higher representation performance.

67 The field of microscopy image analysis can greatly benefit from the development of an
68 unbiased, high-performance, generalist image representation tool. Beyond facilitating accurate
69 downstream analysis, such a tool would enable unsupervised analysis for identifying new
70 phenotypes. It can facilitate the separation of feature extraction and downstream analysis process,
71 allowing for downstream analysis conducted on computers with limited computing power. The
72 representations of images that are much smaller than the original images can be easily stored and
73 transferred, and private data can be shared securely through these representations without disclosing
74 the original images. In addition, secondary analysis becomes possible, such as the creation of large
75 image databases or joint analysis with other data representations. Nevertheless, the complexity and
76 diversity of microscopy images pose significant challenges in the development of such a tool.

77 Self-supervised representation learning offers a promising solution by allowing the model to
78 learn directly from pixels without relying on pre-defined semantic annotations. This approach
79 involves transforming the original images and training the model to learn the mapping between the
80 transformed and original image. Various transformation methods have been employed, such as
81 direct copying¹⁹, partial channel drop²⁰, or image masking²¹, with masked visual representation
82 learning being particularly popular in natural image studies²²⁻²⁴. Recent advancements in cell
83 segmentation algorithms have also indicated the remarkable generalization ability of networks
84 trained on generalized data²⁵⁻²⁷. However, developing a universal tool for microscopy image
85 profiling presents several challenges, including handling images with varying resolutions and
86 channel numbers (such as 1, 2, 3, 5 and 56)^{3-4, 7, 26, 28}, joint representation learning for multiple
87 image styles, processing various image types, and addressing technical variations in high-content
88 experiments that may introduce batch effects in the feature space²⁹⁻³⁰.

89 This study presents Microsnoop, a universal tool for the impartial representation of
90 microscopy images using masked self-supervised learning. The proposed pipeline is capable of
91 handling heterogeneous images and includes a task distribution module to cater to users with
92 varying computing power. To meet diverse image profiling requirements, the images are
93 categorized into three types with corresponding pipelines. The performance of Microsnoop was
94 assessed using seven evaluation datasets from various biological studies and compared against both

95 generalist and custom algorithms. The findings demonstrate Microsnoop's robust feature extraction
96 capabilities and potential for analyzing multi-modal biological data. The tool is freely available at
97 <https://github.com/cellimnet/microsnoop-publish>.
98

99 Results

100 The design of a generalist representation tool.

101 In this study, we developed a generalist tool called Microsnoop for the unbiased representation
102 of microscopy images through masked self-supervised learning. As large and diverse datasets are
103 beneficial for the training of generalist models, we collected and curated 10,458 high-quality
104 microscopy images from various sources published by the cell segmentation community^{25-27, 31-33}.
105 These images were taken using different technologies and have different resolutions and channel
106 numbers, with channels ranging from cellular organelles to tissues. The four main types of images
107 include fluorescence, phase-contrast, tissue and histopathology images (Fig. 1a(i) and
108 Supplementary Table 1). To accommodate the variable number of image channels, the input to the
109 neural network was set as one-channel images (related to one-channel feature concatenation
110 strategy below). All images channels in the training set were split out and further selected to form
111 a one-channel data pool (Methods). Before training, images in each batch were preprocessed in
112 three steps: (1) Sample: randomly select one batch of images from the four types in turn to reduce
113 the effects of unequal amounts of data; (2) Augment: randomly crop a 224*224 region (pad if
114 smaller) from each image, then normalize, random rotate and scale the image, with the result
115 serving as the network target; (3) Transform: randomly mask a portion of the target image patches,
116 with the result serving as the network input. In terms of network architecture design, this study
117 employed a CNN-based³⁴ (convolution neural network) architecture, despite the growing interest
118 in Transformer-based architectures³⁵ for natural image analysis. This choice was motivated by the
119 superior performance observed for the CNN architecture in our preliminary evaluations (Extended
120 Data Fig. 1 and Methods). This performance disparity may be attributed to the difference in the
121 amount of training data provided. Typically, the pre-training of a ViT architecture³⁶ requires a large
122 corpus of data, with over 1 million or even 1 billion images used in the case of natural image
123 studies²¹. However, our microscopy image dataset involved a relatively smaller set of training data,
124 which may not have been sufficient to provide adequate training for the Transformer-based
125 architecture.

126 We employed a masked self-supervised learning strategy to train the network, where a
127 randomly selected percentage of image patches are masked and used as inputs. The network was
128 then tasked with reconstructing the original, unmasked images. During training, masked images are
129 encoded into high-level features through four consecutive downsampling steps, and the process of
130 image reconstruction is accomplished through mirror-symmetric upsampling (Fig. 1a(ii)). The
131 learning process is guided by minimizing the self-supervision loss function (Methods), which
132 promotes the model to learn useful features that enable it to recover the masked parts of the images
133 based on the information present in the remaining parts. This is a challenging task, which
134 necessitates a comprehensive understanding that transcends simple low-level image statistics.

135 At test time, a generalist tool needs to face a range of image processing needs. To cater for this
136 condition, we chose to categorize images based on the image profiling process itself, rather than
137 solely on their biological applications that may be limited in scope. Our categorization comprises
138 three types: single-cell images, fully-imaged images, and batch-experiment images. (Fig. 1b(i)).
139 The images to be processed are first managed by an in-built task distribution module (below), and
140 then fed into the pre-trained encoder on a batch-by-batch basis for feature extraction. The output
141 smallest convolutional maps are processed through global average pooling to produce initial 256-
142 dimensional feature embeddings. Subsequently, feature aggregation is performed in accordance

143 with different profiling tasks (details provided below). The final image representations can be used
144 for various downstream analyses (Fig. 1b(ii)).
145

146 **Diversified evaluation datasets.**

147 In prior studies, attention was primarily focused on a limited number of specific datasets^{5, 37-}
148 ³⁹. In our work, to give a more comprehensive evaluation of our generalist tool, we collected and
149 curated 7 evaluation datasets, encompassing commonly used datasets along with some novel
150 additions, comprising over 358,000 images and 1,270,000 single cells (Methods and Extended Data
151 Fig. 2). These images showcase a diverse array of characteristics, including various resolutions,
152 image types, number of channels, and biological applications, such as protein localization
153 estimation, cell cycle stage identification, and MoA prediction (Supplementary Table 2). In our
154 study, four of the seven evaluation datasets focused on single-cell images. The performance of the
155 model on fluorescent images, including bright-field channels, was assessed by COOS7 Test 1-4³⁹,
156 CYCLOPs³ and BBBC048⁴. For the assessment of the model's ability to handle more challenging
157 histopathology images, we employed the CoNSeP⁴⁰ dataset. The LIVECell Test²⁶ and TissueNet
158 Test²⁷ datasets were designed to evaluate a model's performance on fully-imaged image
159 classification tasks, involving phase-contrast and tissue image representation, respectively. Lastly,
160 the BBBC021⁴¹ dataset was employed to evaluate the representation ability of the model for batch-
161 experiment images.
162

163 **Microsnoop accurately reconstructs the masked input images.**

164 In the investigation of optimal mask ratio for learning features from microscopy images, we
165 found that a 25% mask was optimal for this task. This was determined by testing 8 different mask
166 ratios (5%, 15%, 25%, 35%, 45%, 55%, 65% and 75%) and comparing the results (Extended Data
167 Fig. 3). To get a qualitative sense of the reconstruction task, we showed an example of each image
168 type from the validation set (Fig. 2a). By inputting the 25% masked image into the pre-trained
169 network, we were able to produce a reconstructed image that closely resembles the original, with
170 only some detailed textures lost. This level of detail recovery is not easily achievable by humans.
171 The reconstruction results on single-cell images from the evaluation datasets were even more
172 impressive, with the reconstructed image being nearly indistinguishable from the original image
173 (Fig. 2b and Extended Data Fig. 4). The improved performance on single-cell images in comparison
174 to fully-imaged ones can be attributed to cellular heterogeneity, which results in diverse cell
175 phenotypes. The abundance of reference information from single-cell images allows for the more
176 successful recovery of a limited number of instances. These results demonstrate that the pre-trained
177 Microsnoop network, has learned good representations of the microscopy images.
178

179 **Microsnoop profile of single-cell images with one-channel feature concatenation.**

180 Single-cell images can be produced directly by an imaging instrument such as imaging flow
181 cytometry (IFC)⁴², or obtained through cell segmentation processing on fully-imaged images. To
182 accommodate the variable number of channels, we devised a one-channel feature concatenation
183 strategy (Fig. 3a). Each channel of the multi-channel image is processed independently by
184 Microsnoop, and the resulting embeddings are concatenated in an orderly manner. To prevent
185 confusion during processing, a unique index is assigned to each image when multiple images are
186 being processed. To address potential memory overflow issues when processing large batches of
187 data, we established a task distribution module. This module efficiently manages image pathways
188 and distributes images for processing, read into the CPU and transferred to the GPU as needed. The
189 user is empowered to optimize performance by adjusting parameters according to the available
190 memory capacity of both the CPU and GPU. Furthermore, our system features a scalable,

191 distributed design, which is capable of supporting multiple GPUs, providing a solution for
192 increasing data demands.

193 In our benchmark, we included three previous developed generalist methods in the
194 comparisons: EfficientNetB0⁴³, Inception V3⁴⁴, CytoImageNet¹⁸, and custom methods that are
195 accessible (Methods). For the COOS7 Test 1-4, CYCLoPs and CoNSeP, we evaluated performance
196 with the K-Nearest Neighbor (KNN) classification accuracy (match between prediction and ground
197 truth using the KNN classifier, which has been utilized in prior study¹⁸). For the dataset BBBC048,
198 we used fivefold cross-validation for dataset split and evaluated the performance with the multilayer
199 perceptron (MLP) classification accuracy (match between prediction and ground truth using the
200 MLP classifier, as employed in the original paper⁴). Our evaluations revealed the exceptional
201 performance of Microsnoop, which consistently outperformed all other methods. In the majority of
202 cases, Microsnoop achieved significant improvements of more than 6%, and up to 10% (Fig. 3b-f).
203 Notably, for the 7-classification task of BBBC048, Microsnoop achieved an accuracy of 85.62%
204 without using any data from the dataset, surpassing the custom supervised learning algorithm in the
205 original paper by 5.02%.

206 207 **Microsnoop profile of fully-imaged images with cell region cropping.**

208 Fully-imaged images are a common format directly obtained from most microscopes. Cell
209 segmentation is usually the first step of phenotype profiling due to the inherent heterogeneity of
210 cells. Although various generalist segmentation algorithms²⁵⁻²⁷ have been developed along with
211 some fine-tuning strategies⁴⁵⁻⁴⁶, they may still introduce unwanted segmentation errors. For
212 instance, in a large drug screening experiment, cell body images can present a range of phenotypes,
213 and a segmentation algorithm may perform well on some but poorly on others (Extended Data Fig.
214 5a), potentially leading to unpredictable impacts on downstream analysis. To mitigate these issues,
215 we introduced a cell region cropping strategy, where the segmentation algorithm is applied only on
216 the easiest channel, such as the nucleus channel, which presents more robust segmentation results
217 (Extended Data Fig. 5b). Cell regions are computed and cropped based on the segmentation masks
218 and rescale constant (Fig. 4a(i) and Methods). Then, Microsnoop extracts features from the cropped
219 single-cell images as described above (Fig. 4a(ii)). Finally, the resulting single-cell level
220 embeddings are aggregated by computing their mean to obtain the fully-imaged level
221 representations (Fig. 4a(iii)).

222 We evaluated the representation ability of Microsnoop on two fully-imaged image phenotype
223 classification tasks, and tested previously mentioned generalist algorithms for comparison. Both
224 tasks were evaluated using the KNN classification accuracy. The results showed that Microsnoop
225 again outperformed other methods, and even a 41.93% improvement was obtained on the LIVECell
226 Test dataset (Fig. 4b-c). Furthermore, Microsnoop showed strong inclusiveness to various image
227 styles, with an accuracy of 98.08% on the LIVECell Test dataset and 96.64% on TissueNet Test.

228 229 **Microsnoop profile of batch-experiment images with spherling batch correction.**

230 In high-content screening experiments, batch effects due to technical variability can affect
231 downstream analysis^{29-30, 37-38} (Fig. 5a). To address this issue, we employed a spherling batch
232 correction method⁴⁷. This assumes that the large variations observed in negative controls are
233 associated with confounders, and any variation that is not observed in controls is associated with
234 phenotypes. Spherling transformation aims to separate phenotypic variation from confounders. In
235 our image representation pipeline for batch-experiment images, Microsnoop first extracts features
236 from the fully-imaged images (as described above), and the resulting fully-imaged level
237 representations are corrected via spherling transformation (Fig. 5b). Finally, the fully-imaged level
238 representations are aggregated to treatment level representations by computing their mean (Fig. 5c).

239 We evaluated the representation ability of Microsnoop on the classic BBBC021 dataset, while
240 including previously reported results of generalist and custom methods in the comparisons. We
241 assessed the performance with the Not-Same-Compound (NSC) and Not-Same-Compound-or-
242 Batch (NSCB) KNN classification accuracy. Microsnoop still achieved state-of-the-art
243 performance without using any data from the dataset, even if compared with the methods
244 exclusively studied on it (Fig. 5d-e).

245
246 **Two other fully-imaged image profile modes and the robustness of cell region cropping mode.**

247 In addition to the cell region cropping mode, we provided two alternative modes for processing
248 fully-imaged datasets: rescaling and tile mode. In the rescaling mode, the shape of the fully-imaged
249 images is directly rescaled to the input size (224*224) as inputs (Extended Data Fig. 6a-b). In the
250 tile mode, the original image is cropped into multiple 224x224 tiles, and the fully-imaged level
251 representations are aggregated by computing the mean over all tiles (Extended Data Fig. 6c). We
252 evaluated the performance of these three processing modes, including different rescale constants
253 for the cell region cropping mode, on both the fully-imaged and batch-experiment datasets
254 (Extended Data Fig. 6d-g and Methods). The rescaling and tile modes outperformed the single-cell
255 mode on LIVECell and TissueNet tests; however, both modes displayed a significant performance
256 decline on the BBBC021 dataset. The reason for the underperformance of the rescaling mode could
257 be attributed to the fact that it discards high-resolution phenotypic information during the rescaling
258 process. On the other hand, the decline in performance observed with the tile mode may be due to
259 the fact that it averages out important subtle phenotype variations present in certain regions of fully-
260 imaged images. In contrast, the cell region cropping mode displayed robust performance across a
261 range of parameters on all three datasets. Although the single-cell mode is more robust and efficient,
262 it requires more time and memory compared to the other two modes. (Extended Data Fig. 6h-i).

263
264 **Microsnoop improves the performance of the multi-modal structured embedding algorithm.**

265 A recent study of the multi-modal structured embedding algorithm (MUSE¹⁷) has shown
266 impressive results for the integrative spatial analysis of image and transcriptional data. The authors
267 conducted a simulation experiment to assess the performance of MUSE when transcriptional data
268 quality is degraded. Here, we focused on the impact of image feature quality, and the results of our
269 simulation experiment showed that with the quality improvement of image representations, the
270 performance of MUSE can also be significantly improved (Extended Data Fig. 7). Next, we tested
271 Microsnoop on the real-world dataset seqFISH+⁸ in comparison with the representation method
272 used in the original paper. After acquiring the image representations, we use principal component
273 analysis (PCA) performing feature dimensionality reduction to match the latent space dimensions
274 of MUSE (Fig. 6a). We employed the silhouette coefficient⁴⁸ to evaluate the feature quality.
275 Microsnoop demonstrated better image representation quality and greater improvement in the
276 performance of MUSE (Fig. 6b).

277
278 **Discussion**

279 Advances in imaging technology, such as phase-contrast microscopy, imaging flow cytometry,
280 automated high-throughput microscopy and microscopy combined with spatial omics techniques
281 have created a massive demand to solve the complex challenge of microscopy image representation.
282 In this study, we present Microsnoop, an innovative deep learning tool that effectively addresses
283 this challenge. The accurate analysis of heterogeneous microscopy images, as a critical aspect of
284 both fundamental and applied biological research, is highly valued by the microscopy image
285 analysis community⁴⁹⁻⁵⁰. Our proposed solution offers promising advancements to this field.
286 Microsnoop was trained on large-scale high-quality data using a masked self-supervised pretext
287 task, allowing it to learn valuable and unbiased features for image representation. The one-channel

288 feature concatenation strategy, efficient task distribution module, and rational classification mode
289 of profiling needs make our tool flexible to meet various user needs. In addition, Microsnoop is
290 capable of processing complex fully-imaged images through cell region cropping and mitigating
291 batch effects in batch-experiment images through spherling transformation. For fully-imaged
292 images, our results show that the single-cell analysis mode is more robust compared to other modes,
293 reinstating the importance of considering cellular heterogeneity in biological research. Our
294 benchmark results demonstrate robust and state-of-the-art performance on all evaluated datasets,
295 eliminating the need to use of any evaluation data for fine-tuning. Furthermore, the enhanced
296 representation of unimodal image data leads to significant improvements in the performance of
297 multi-modal algorithms.

298 In our methodology experiments, we found that a mask ratio of 25% is optimal for microscopy
299 images, which is significantly lower than the 75% that has been found optimal for natural images²¹.
300 The difference is primarily due to the smaller size and erratic content of instances in microscopy
301 images, which may result in lost information if too much reference information is masked.
302 Compared with the CytoImageNet¹⁸ study that utilized a supervised classification task as the pretext
303 task, our masked self-supervised learning approach only requires raw images without any manual
304 annotation and yields unbiased and more capable representations. Recently, a similar self-
305 supervised representation learning study has also been reported as useful in learning the
306 representations of protein subcellular location images through a pretext task that requires the
307 network to directly reconstruct original images and images corresponding to similar proteins having
308 similar representations¹⁹. In contrast, the uniqueness of our method is that ours do not require
309 domain-specific knowledge and is developed for generalist image representation. Our benchmark
310 study has shown that a single network is capable of handling heterogeneous microscopy images,
311 which is in line with the conclusion reached in the sister domain of cell segmentation²⁵. Furthermore,
312 our pretext task was trained on the same network structure as Cellpose. This is reminiscent of the
313 recent success of large pre-trained language models in the field of natural language processing⁵¹⁻
314 ⁵³. With continued advancements in the understanding of computer vision and the further
315 development of models for microscopy image representation and other image processing tasks,
316 such as cell segmentation, it may be possible to merge these models into a single, unified model in
317 the future.

318 While Microsnoop is a powerful tool, there are several areas for improvement. For example,
319 further evaluation is needed to determine the efficacy of our approach of one-channel feature
320 concatenation and feature aggregation in 3D and time-series imaging datasets in comparison to
321 training a network to directly extract spatial or temporal information. To enhance the capabilities
322 of Microsnoop, future work could include incorporating additional self-supervised pretext tasks for
323 multi-task learning, optimizing the quality of the training dataset and refining the single-cell level
324 feature aggregation methods. Moreover, the current training images are still limited in size
325 compared to natural images, and a larger training data volume combined with the Transformer
326 architecture can be studied to improve the performance. Last but not least, deploying our model on
327 mobile devices to aid rapid detection could be a valuable application scenario⁵⁴.

328 Overall, we have developed an impressive, generalist tool for microscopy image
329 representation. We anticipate its positive impact on the microscopy image analysis community,
330 facilitating new phenotype discovery, data sharing, and the establishment of large image databases,
331 among other benefits. Furthermore, we envision that Microsnoop can be effectively utilized in
332 multi-modal studies such as combining molecular and image representation for MoA prediction⁵⁵⁻
333 ⁵⁶ or exploring the relationship between gene expression, image representation for drug discovery⁵⁷
334 and much broader applications⁵⁸⁻⁵⁹.

336 References

- 337 1. Caicedo, J. C., Singh, S. & Carpenter, A. E. Applications in image-based profiling of
338 perturbations. *Curr. Opin. Biotechnol.* **39**, 134-142 (2016).
- 339 2. Pratapa, A., Doron, M. & Caicedo, J. C. Image-based cell phenotyping with deep learning. *Curr.*
340 *Opin. Chem. Biol.* **65**, 9-17 (2021).
- 341 3. Lu, A. X. et al. Integrating images from multiple microscopy screens reveals diverse patterns
342 of change in the subcellular localization of proteins. *eLife* **7**, e31872 (2018).
- 343 4. Eulenberg, P. et al. Reconstructing cell cycle and disease progression using deep learning. *Nat.*
344 *Commun.* **8**, 463 (2017).
- 345 5. Pawlowski, N., Caicedo, J. C., Singh, S., Carpenter, A. E. & Storkey, A. Automating
346 Morphological Profiling with Generic Deep Convolutional Networks. Preprint at
347 <http://biorxiv.org/lookup/doi/10.1101/085118> (2016).
- 348 6. Cuccarese, M. F. et al. Functional immune mapping with deep-learning enabled phenomics
349 applied to immunomodulatory and COVID-19 drug discovery. Preprint at
350 <http://biorxiv.org/lookup/doi/10.1101/2020.08.02.233064> (2020).
- 351 7. Schürch, C. M. et al. Coordinated Cellular Neighborhoods Orchestrate Antitumoral Immunity
352 at the Colorectal Cancer Invasive Front. *Cell* **182**, 1341-1359 (2020).
- 353 8. Eng, C.-H. L. et al. Transcriptome-scale super-resolved imaging in tissues by RNA seqFISH+.
354 *Nature* **568**, 235-239 (2019).
- 355 9. Carpenter, A. E. et al. CellProfiler: image analysis software for identifying and quantifying cell
356 phenotypes. *Genome Biol.* **7**, R100 (2006).
- 357 10. Pau, G., Fuchs, F., Sklyar, O., Boutros, M. & Huber, W. EBImage--an R package for image
358 processing with applications to cellular phenotypes. *Bioinformatics* **26**, 979-981 (2010).
- 359 11. Singh, S., Bray, M.-A., Jones, T. R. & Carpenter, A. E. Pipeline for illumination correction of
360 images for high-throughput microscopy. *J. Microsc.* **256**, 231-236 (2014).
- 361 12. Caicedo, J. C., McQuin, C., Goodman, A., Singh, S. & Carpenter, A. E. Weakly Supervised
362 Learning of Single-Cell Feature Embeddings. In *Proc. IEEE Conference on Computer Vision*
363 *and Pattern Recognition* 9309-9318 (IEEE, 2018).
- 364 13. Lu, A. X., Kraus, O. Z., Cooper, S. & Moses, A. M. Learning unsupervised feature
365 representations for single cell microscopy images with paired cell inpainting. *PLoS Comput.*
366 *Biol.* **15**, e1007348 (2019).
- 367 14. Adnan, M., Kalra, S. & Tizhoosh, H. R. Representation Learning of Histopathology Images
368 Using Graph Neural Networks. In *Proc. IEEE Conference on Computer Vision and Pattern*
369 *Recognition* 988-989 (IEEE, 2020).
- 370 15. Perakis, A. et al. Contrastive Learning of Single-Cell Phenotypic Representations for Treatment
371 Classification. In *Machine Learning in Medical Imaging* (eds. Lian, C., Cao, X., Rekik, I., Xu,
372 X. & Yan, P.) **12966**, 565-575 (Springer, 2021).
- 373 16. Russakovsky, O. et al. ImageNet Large Scale Visual Recognition Challenge. *Int. J. Comput. Vis.*
374 **115**, 211-252 (2015).
- 375 17. Bao, F. et al. Integrative spatial analysis of cell morphologies and transcriptional states with
376 MUSE. *Nat. Biotechnol.* **40**, 1200-1209 (2022).
- 377 18. Hua, S. B. Z., Lu, A. X. & Moses, A. M. CytoImageNet: A large-scale pretraining dataset for
378 bioimage transfer learning. In *Proc. Advances in Neural Information Processing Systems*
379 (Curran Associates, 2021).
- 380 19. Kobayashi, H., Cheveralls, K. C., Leonetti, M. D. & Royer, L. A. Self-supervised deep learning
381 encodes high-resolution features of protein subcellular localization. *Nat. Methods* **19**, 995-1003
382 (2022).
- 383 20. Wong, D. R. et al. Trans-channel fluorescence learning improves high-content screening for
384 Alzheimer's disease therapeutics. *Nat. Mach. Intell.* **4**, 583-595 (2022).
- 385 21. He, K. et al. Masked Autoencoders Are Scalable Vision Learners. In *Proc. IEEE Conference on*

386 *Computer Vision and Pattern Recognition* 16000-16009 (IEEE, 2022).

387 22. Liu, X., Zhou, J., Kong, T., Lin, X. & Ji, R. Exploring Target Representations for Masked
388 Autoencoders. Preprint at <https://arxiv.org/abs/2209.03917> (2022).

389 23. Li, Z. et al. MST: Masked Self-Supervised Transformer for Visual Representation. In *Proc.*
390 *Advances in Neural Information Processing Systems* 35 (Curran Associates, 2021).

391 24. Wei, C. et al. Masked Feature Prediction for Self-Supervised Visual Pre-Training. In *Proc. IEEE*
392 *Conference on Computer Vision and Pattern Recognition* 14668-14678 (IEEE, 2022).

393 25. Stringer, C., Wang, T., Michaelos, M. & Pachitariu, M. Cellpose: a generalist algorithm for
394 cellular segmentation. *Nat. Methods* **18**, 100-106 (2021).

395 26. Edlund, C. et al. LIVECell-A large-scale dataset for label-free live cell segmentation. *Nat.*
396 *Methods* **18**, 1038-1045 (2021).

397 27. Greenwald, N. F. et al. Whole-cell segmentation of tissue images with human-level performance
398 using large-scale data annotation and deep learning. *Nat. Biotechnol.* **40**, 555-565 (2021).

399 28. Bray, M.-A. et al. Cell Painting, a high-content image-based assay for morphological profiling
400 using multiplexed fluorescent dyes. *Nat. Protoc.* **11**, 1757-1774 (2016).

401 29. Leek, J. T. et al. Tackling the widespread and critical impact of batch effects in high-throughput
402 data. *Nat. Rev. Genet.* **11**, 733-739 (2010).

403 30. Lin, A. & Lu, A. X. Incorporating knowledge of plates in batch normalization improves
404 generalization of deep learning for microscopy images. In *Proc. International Conference on*
405 *Machine Learning* 74-93 (PMLR, 2022).

406 31. Kumar, N. et al. A Multi-Organ Nucleus Segmentation Challenge. *IEEE Trans. Med. Imaging*.
407 **39**, 1380-1391 (2020).

408 32. Verma, R. et al. MoNuSAC2020: A Multi-Organ Nuclei Segmentation and Classification
409 Challenge. *IEEE Trans. Med. Imaging*. **40**, 3413-3423 (2021).

410 33. Amgad, M. et al. NuCLS: A scalable crowdsourcing, deep learning approach and dataset for
411 nucleus classification, localization and segmentation. *Gigascience* **11**, giac037 (2022).

412 34. Ronneberger, O., Fischer, P. & Brox, T. U-Net: Convolutional Networks for Biomedical Image
413 Segmentation. In *Proc. International Conference on Medical Image Computing and Computer-*
414 *Assisted Intervention* 234-241 (Springer, 2015).

415 35. Vaswani, A. et al. Attention is All you Need. In *Proc. Advances in Neural Information*
416 *Processing Systems* 30 (Curran Associates, 2017).

417 36. Dosovitskiy, A. et al. An Image is Worth 16x16 Words: Transformers for Image Recognition at
418 Scale. In *International Conference on Learning Representations* (ICLR, 2021).

419 37. Ando, D. M., McLean, C. Y. & Berndl, M. Improving Phenotypic Measurements in High-
420 Content Imaging Screens. Preprint at <http://biorxiv.org/lookup/doi/10.1101/161422> (2017).

421 38. Bray, M.-A. et al. High-content cellular screen image analysis benchmark study. Preprint at
422 <https://www.biorxiv.org/content/10.1101/2022.05.15.491989v1.abstract> (2022).

423 39. Lu, A. et al. The Cells Out of Sample (COOS) dataset and benchmarks for measuring out-of-
424 sample generalization of image classifiers. In *Proc. Advances in Neural Information Processing*
425 *Systems* 32 (Curran Associates, 2019).

426 40. Graham, S. et al. Hover-Net: Simultaneous segmentation and classification of nuclei in multi-
427 tissue histology images. *Med. Image Anal.* **58**, 101563 (2019).

428 41. Caie, P. D. et al. High-Content Phenotypic Profiling of Drug Response Signatures across
429 Distinct Cancer Cells. *Mol. Cancer Ther.* **9**, 1913-1926 (2010).

430 42. Schraivogel, D. et al. High-speed fluorescence image-enabled cell sorting. *Science* **375**, 315-
431 320 (2022).

432 43. Tan, M. & Le, Q. V. EfficientNet: Rethinking Model Scaling for Convolutional Neural
433 Networks. In *Proc. International Conference on Machine Learning* 6105-6114 (PMLR, 2019).

434 44. Szegedy, C., Vanhoucke, V., Ioffe, S., Shlens, J. & Wojna, Z. Rethinking the Inception
435 Architecture for Computer Vision. In *Proc. IEEE Conference on Computer Vision and Pattern*

436 *Recognition* 2818-2826 (IEEE, 2016).

437 45. Xun, D. et al. Scellseg: A style-aware deep learning tool for adaptive cell instance segmentation
438 by contrastive fine-tuning. *iScience* **25**, 105506 (2022).

439 46. Pachitariu, M. & Stringer, C. Cellpose 2.0: how to train your own model. *Nat. Methods* **19**,
440 1634-1641 (2022).

441 47. Moshkov, N. et al. Learning representations for image-based profiling of perturbations. Preprint
442 at <http://biorxiv.org/lookup/doi/10.1101/2022.08.12.503783> (2022).

443 48. Rousseeuw, P. J. Silhouettes: A graphical aid to the interpretation and validation of cluster
444 analysis. *J. Comput. Appl. Math.* **20**, 53-65 (1987).

445 49. Caicedo, J. C. et al. Data-analysis strategies for image-based cell profiling. *Nat. Methods* **14**,
446 849-863 (2017).

447 50. Chandrasekaran, S. N., Ceulemans, H., Boyd, J. D. & Carpenter, A. E. Image-based profiling
448 for drug discovery: due for a machine-learning upgrade? *Nat. Rev. Drug. Discov.* **20**, 145-159
449 (2020).

450 51. Devlin, J., Chang, M.-W., Lee, K. & Toutanova, K. BERT: Pre-training of Deep Bidirectional
451 Transformers for Language Understanding. Preprint at <https://arxiv.org/abs/1810.04805> (2018).

452 52. Brown, T. B. et al. Language Models are Few-Shot Learners. In *Proc. Advances in Neural*
453 *Information Processing Systems* 33 (Curran Associates, 2020).

454 53. Min, B. et al. Recent Advances in Natural Language Processing via Large Pre-Trained
455 Language Models: A Survey. Preprint at <http://arxiv.org/abs/2111.01243> (2021).

456 54. Wang, B. et al. Smartphone-based platforms implementing microfluidic detection with image-
457 based artificial intelligence. *Nat. Commun.* **14**, 1341 (2023).

458 55. Sanchez-Fernandez, A., Rumetschofer, E. & Hochreiter, S. CONTRASTIVE LEARNING OF
459 IMAGE- AND STRUCTURE- BASED REPRESENTATIONS IN DRUG DISCOVERY. In
460 *International Conference on Learning Representations* (ICLR, 2022).

461 56. Tian, G., Harrison, P. J., Sreenivasan, A. P., Puigvert, J. C. & Spjuth, O. Combining molecular
462 and cell painting image data for mechanism of action prediction. Preprint at
463 <http://biorxiv.org/lookup/doi/10.1101/2022.10.04.510834> (2022).

464 57. Haghghi, M., Caicedo, J. C., Cimini, B. A., Carpenter, A. E. & Singh, S. High-dimensional
465 gene expression and morphology profiles of cells across 28,000 genetic and chemical
466 perturbations. *Nat. Methods* **19**, 1550-1557 (2022).

467 58. Liu, L., Bi, M., Wang, Y., Liu, J., Jiang, X., Xu, Z. and Zhang, X. Artificial intelligence-
468 powered microfluidics for nanomedicine and materials synthesis. *Nanoscale* **13**(46), 19352-
469 19366 (2021).

470 59. Wang, X., Xie, P., Chen, B. and Zhang, X. Chip-based high-dimensional optical neural network.
471 *Nano-Micro Lett.* **14**(1), 221 (2022).

472 60. Ljosa, V., Sokolnicki, K. L. & Carpenter, A. E. Annotated high-throughput microscopy image
473 sets for validation. *Nat. Methods* **9**, 637-637 (2012).

474 61. Hubert, L. & Arabie, P. Comparing partitions. *J. Classif.* **2**, 193-218 (1985).

475 62. Schneider, C. A., Rasband, W. S. & Eliceiri, K. W. NIH Image to ImageJ: 25 years of image
476 analysis. *Nat. Methods* **9**, 671-675 (2012).

477 63. Paszke, A. et al. PyTorch: An Imperative Style, High-Performance Deep Learning Library. In
478 *Proc. Advances in Neural Information Processing Systems* 32 (Curran Associates, 2019).

479 Methods

480 Training set.

481 The training set consisted of four diverse image types from seven published datasets: Cellpose,
482 LIVECell, TissueNet, and Histo, which includes MoNuSeg, MoNuSAC, and NuCLS. Firstly, all
483 channels of the images were separated. For Cellpose and TissueNet, only the cell body channel was
484 utilized, while the original RGB images of Histo were transformed into grayscale. The original
485 training-validation dataset split was maintained for Cellpose, LIVECell, and TissueNet, while the
486 images from the three Histo subsets were mixed and 20% were randomly reserved for validation
487 purposes. Finally, the training set was organized into a one-channel image data pool. A
488 comprehensive summary of the training set can be found in Supplementary Table 1.

489 Model architecture.

490 The network architecture was based on a refined version of the classic U-Net³⁴, as utilized in
491 Cellpose. The standard convolutional blocks were replaced with residual blocks and style
492 embeddings were incorporated into the concatenation stages. The downsampling scale was set as
493 32, 64, 128 and 256, and the upsampling scale was mirror symmetry. Both the input and output
494 tensors were of shape batch_size*1*224*224 (in Pytorch tensor format, where batch_size is
495 described below).

496 Masked self-supervised learning.

497 In the masked self-supervised learning approach, the network is tasked with reconstructing the
498 original image from partial masked images. Our implementation involved dividing the target image
499 (after normalization and augmentation) into 16*16 non-overlapping patches. Subsequently, a
500 portion of these patches were randomly replaced with black patches of size 16*16, where every
501 pixel was zero. Different from the original MAE built on a Transformer architecture, the
502 transformed patches were restored to the image format to accommodate the input format of the
503 CNN architecture.

504 Model training.

505 The self-supervision loss was set as the mean square error loss (MSE), which calculates the
506 difference in both the masked and unmasked areas. The network was optimized by AdamW
507 optimizer from the torch.optim Python package. In our implementation, we adopted a different
508 definition of an epoch, in which one epoch corresponds to a complete iteration through all the
509 sampled data, rather than through all the training data, as is commonly defined. During each epoch,
510 we randomly sampled 12000 images from the four different types of training data in turn. The batch
511 size was set as 16. The initial learning rate was set as 0.001, and we used a learning rate (LR)
512 warmup trick: at the first 40 epochs, the LR was computed as:

$$513 \quad \text{LR} = 0.001 * \frac{\text{epoch}}{40}$$

514 after 40 epochs, the LR was computed as:

$$515 \quad \text{LR} = 0.001 * 0.5 * [1 + \cos\left(\frac{\text{epoch} - 40}{\text{nepoch} - 40} * \pi\right)]$$

516 where nepoch represents the epoch size of the training process, here it was set as 1000.

517 One-channel feature concatenation strategy for multi-channel image representation.

518 In our implementation of Microsnoop for feature extraction, we assumed that the input data
519 comprised multi-channel images with the same number of channels, represented as (c, h, w), where
520 c denotes the number of channels, and h and w denote the height and width, respectively. In the
521 event that images had different h and w, we padded them with zeros to obtain a consistent shape.
522 The task distribution module is then used to read the images into CPU memory, where they are

527 transformed into an array with shape (n, c, h, w), where n denotes the number of images read. This
528 array is then reshaped into (n*c, 1, h, w), with each image assigned a unique index represented as
529 a shape (n*c,) vector. For each batch of size b, the task distribution module transfers b images into
530 the GPU memory, resulting in a tensor of shape (b, 1, h, w). After Microsnoop processes all n*c
531 images, the CPU cache is cleared using the collect function from the gc Python package, and the
532 next n images are read. The resulting embedding array had the shape of (N*c, 256), where N denotes
533 the total number of processed images, and 256 is the pre-set dimensionality of the feature vector
534 for a one-channel image in Microsnoop. These embeddings are then concatenated in channel to
535 obtain a final feature embedding array of shape (N, 256*c).

536

537 Evaluation datasets.

538 We curated seven evaluation datasets, four of which were directly available from public
539 sources and three (CoNSeP, LIVECell Test and TissueNet Test) were processed by us based on
540 publicly acquired images. The summary of these datasets can be seen in Supplementary Table 2.

541

542 *COOS7*. This dataset contains 132,209 single-cell fluorescence images, including a training set and
543 four test sets that vary in different factors. The training set consists of images from 4 independent
544 plates, while Test 1 includes randomly held-out images from the same plates as the training set,
545 Test 2 includes images from the same plates but different wells, Test3 comprises images produced
546 months later, and Test 4 has images produced by other instruments. The images were downloaded
547 through the link provided by Stanley Bryan Z. Hua¹⁸. Each image takes the shape of 2*64*64 and
548 is a pixel crop centered around a unique mouse cell. One channel marks the protein targeting a
549 specific component of the cell and the other marks the nucleus. There are 7 protein location classes
550 in each set: Endoplasmic Reticulum, Inner Mitochondrial Membrane, Golgi, Peroxisomes, Early
551 Endosome, Cytosol and Nuclear Envelope, and the evaluation task requires the model to accurately
552 predict the protein location.

553

554 *CYCLoPs*. This dataset consists of 28,166 single-cell fluorescence images from the CYCLoPs
555 database, and we downloaded the data through the link provided by Stanley Bryan Z. Hua¹⁸. Each
556 image has a shape of 2*64*64 and is a pixel crop centered around a unique yeast cell. One channel
557 marks the protein location and the other marks the cytosol. There are 17 protein location classes:
558 ACTIN, BUDNECK, BUDTIP, CELLPERIPHERY, CYTOPLASM, ENDOSOME, ER, GOLGI,
559 MITOCHONDRIA, NUCLEARPERIPHERY, NUCLEI, NUCLEOLUS, PEROXISOME,
560 SPINDLE, SPINDLEPOLE, VACUOLARMEMBRANE and VACUOLE. The aim of the
561 evaluation is to accurately predict the protein localization.

562

563 *CoNSeP*. This dataset has 41 H&E stained fully-imaged images with a shape of 3*1000*1000 pixels.
564 14 of these are test images and 27 are training images. The raw data were obtained from
565 <https://warwick.ac.uk/fac/sci/dcs/research/tia/data> and then transformed into grayscale format.
566 Each cell was cropped based on the provided segmentation mask, resulting in 8777 single-cell test
567 images and 15554 single-cell training images with a shape of 1*112*112 pixels. In cases where the
568 cells were smaller, padding was applied to obtain the desired size. The class information was
569 extracted from the classification mask, with 4 classes: Other, Inflammatory, Epithelial, Spindle-
570 shaped. The evaluation task requires the model to accurately predict the cell types.

571

572 *BBBC048*. This dataset contains 32,266 single-cell images from the Broad Bioimage Benchmark
573 Collection⁶⁰. These single-cell images of Jurkat cells were directly captured with the ImageStream
574 imaging flow cytometer. Each image has a shape of 3*66*66 pixels, with a brightfield channel and
575 two fluorescence channels. There are 7 cell phases: G1, S, G2, Prophase, Metaphase, Anaphase and

576 Telophase. Another 5-phase case considers G1, S and G2 phase as a single class. The evaluation
577 task requires the model to accurately predict the cell cycle stages.
578

579 *LIVECell Test.* This dataset comprises 1512 fully-imaged phase-contrast images provided by
580 Christoffer Edlund²⁶, where each image has a shape of 1*520*704 pixels. There are 8 cell types:
581 A172, BT474, BV2, Huh7, MCF7, SHSY5Y, SkBr3 and SKOV3. The evaluation task requires the
582 model to accurately predict the cell types of full-imaged images.
583

584 *TissueNet Test.* This dataset comprises 1249 fully-imaged tissue images provided by Noah F.
585 Greenwald. Each image has a shape of 2*256*256 pixels, one channel marks the membrane or
586 cytoplasm and the other marks the nucleus. We extracted the tissue type information from the
587 metadata provided. There are 6 tissue types: Breast, Gi, Immune, Lung, Pancreas and Skin. The
588 evaluation task requires the model to accurately predict the tissue types of full-imaged images.
589

590 *BBBC021.* This dataset includes 3848 fully-imaged fluorescence images, a subset from the Broad
591 Bioimage Benchmark Collection⁶⁰. The images are of MCF-7 breast cancer cells with a collection
592 of 113 small molecules at different concentrations and a DMSO negative control. Each image has
593 a shape of 3*1024*1280 pixels, and different channels respectively mark the DNA, F-actin and B-
594 tubulin. There are 12 mechanisms: Actin disruptors, Aurora kinase inhibitors, Cholesterol-lowering,
595 DNA damage, DNA replication, Eg5 inhibitors, Epithelial, Kinase inhibitors, Microtubule
596 destabilizers, Microtubule stabilizers, Protein degradation and Protein synthesis. The evaluation
597 task requires the model to accurately predict the MoA of different treatments.
598

599 **Three modes for the profile of fully-imaged images.**

600 *Cell region cropping mode.* We utilized the generalist tool Cellpose on the easiest channel (such as
601 the nucleus channel) to perform cell segmentation. For each image, following the acquisition of the
602 segmentation mask, we extract all the (x, y) pixel coordinates of each cell, and compute the region
603 of each cell as follows:

$$\begin{aligned} 604 \quad w &= x_{max} - x_{min} ; \quad h = y_{max} - y_{min} \\ 605 \quad x_c &= x_{min} + 0.5 * w ; \quad y_c = y_{min} + 0.5 * h \\ 606 \quad Rs &= \min(\max(w, h) * Rc, Sta * 0.5) \\ 607 \quad bbox_0 &= \max(x_c - Rs, 0) ; \quad bbox_1 = \max(y_c - Rs, 0) \\ 608 \quad bbox_2 &= \min(x_c + Rs, W) ; \quad bbox_3 = \min(y_c + Rs, H) \end{aligned}$$

609 where $x_{max}, x_{min}, y_{max}, y_{min}$ denote the max/min x/y, respectively, among all the pixels
610 coordinates; x_c, y_c denote the coordinates of centroid; Rc denotes the rescale constant (it is set by
611 user according to the average size of cell bodies); Sta denotes the side length of cropped image
612 (here we set it as 224, the input size of Microsnoop); Rs denotes the crop size (it cannot be more
613 than half of Sta); W, H denote the width and height of the fully-imaged image, respectively.
614 $bbox_0, bbox_1, bbox_2, bbox_3$ denote the left, up, right, down of the cropped region in the original
615 image, respectively, and they cannot go beyond the boundaries of the image. Finally, single-cell
616 images are cropped on all channels and padded to (c, Sta , Sta) with zero pixels if smaller, where c
617 denotes the number of channels. The fully-imaged level embedding of the image is obtained by
618 computing the mean of all single-cell image embeddings.
619

620 *Rescaling mode.* In the case that the height of the image is not equal to its width, the initial step is
621 to pad the image with zeros to create a square shape. The fully-imaged images are then rescaled to
622 input size using the resize function from the cv2 Python package. The fully-imaged level
623 embedding of the image is directly obtained through this process.
624

625 *Tile mode.* The fully-imaged images are cropped into tiles using the make_tiles function from the
626 cellpose.transforms Python package. The parameter bsize was set as the input size, and the
627 parameter tile_overlap was set as 0.1. The fully-imaged level embedding of the image is obtained
628 by computing the mean of all tile embeddings.

629 **Spherling transformation for the profile of batch-experiment images.**

630 The detailed description can be found in ref.⁴⁷. Here, we fitted the ZCA_corr transformer from
631 [https://github.com/jump-
632 cellpainting/2021_Chandrasekaran_submitted/blob/main/benchmark/old_notebooks/utils.py](https://github.com/jump-cellpainting/2021_Chandrasekaran_submitted/blob/main/benchmark/old_notebooks/utils.py) on
633 the embeddings of negative control, and then used the fitted transformer to correct the embeddings
634 of each batch.

635 **Benchmarking.**

636 For BBBC021, we directly adopted the previously published state-of-the-art (SOTA) results
637 from the curated resource at <https://bbbc.broadinstitute.org/BBBC021>. We also included the results
638 of recently reported generalist methods. All results were formatted to two decimal places.

639 For other datasets, we compared with three generalist deep-learning methods:
640 EfficientNetB0, Inception V3 and CytoImageNet. EfficientNetB0 was pretrained on the
641 ImageNet and was included in the comparison in CytoImageNet. The famous project DeepProfiler⁴⁷
642 also used this network for the profiling of microscopy imaging data. Inception V3, which was also
643 pre-trained on ImageNet, had been utilized in the MUSE project, a study of advanced multimodal
644 algorithms. CytoImageNet, a recently published generalist microscopy image representation
645 learning algorithm, was pre-trained using a self-constructed microscopy image classification
646 dataset.

647 The results of EfficientNetB0 and CytoImageNet on COOS7 and CYCLOPs have been
648 previously reported¹⁸ and were directly adopted from the relevant publication. For BBBC048, we
649 also included the custom algorithm results reported in the original paper. The remaining results
650 presented in this paper were generated by the authors.

651 EfficientNetB0 and CytoImageNet were established using the EfficientNetB0 class from
652 the tensorflow.keras.applications Python package, with different weights loaded
653 (EfficientNetB0 used the ImageNet weights and CytoImageNet used the weights published by
654 Stanley Bryan Z. Hua). Inception V3 was established using inception_v3 class from the
655 torchvision.models Python package. We dropped the last classification layer and used the remaining
656 network for feature extraction. Because these network architectures are presented in natural RGB
657 image study, at test time, each one-channel image is copied three times to mimic RGB images (also
658 used in ref.^{18, 37}). The other steps, such as data preprocessing and feature aggregation, are identical
659 to those used in the Microsnoop protocol.

660 For LIVECell and TissueNet Test, we directly used the provided segmentation masks (nucleus
661 channel for the TissueNet) without applying the cell segmentation algorithm in the cell region
662 cropping mode. For the COOS7, CYCLOPs and BBBC021 datasets, the number of nearest
663 neighbors (k) in the KNN classifier was set to 11, 11, and 1, respectively, in accordance with the
664 ref.¹⁸. For BBBC048, the MLP was conducted using the MLPClassifier class from the
665 sklearn.neural_network Python package, and the parameter max_iter was set as 1000.

666 **Joint use of Microsnoop and MUSE.**

667 In the simulation experiment, we utilized the simulation_tool.multi_modal_simulator function
668 from the MUSE project to generate the transcriptional and image representations along with the
669 corresponding ground truth. We used the adjusted Rand index (ARI)⁶¹ to assess the ability of
670 discovering true subpopulations. For the analysis of seqFISH+ data, the microscopy images were
671 provided by the authors of the seqFISH+ paper. Each cell region of the images was determined by

675 the coordinates of the cell centroid provided. We used Microsnoop and Inception V3 to conduct
676 feature extraction on the Nissl and DAPI stained images separately. The shape of each single-cell
677 embedding output was 512 (256*2), then we used PCA to reduce the feature dimensionality to 500.
678 The process of the transcript data was the same as MUSE. We used the silhouette coefficient to
679 assess feature quality by the compactness of the clusters, which was conducted using the
680 silhouette_score function from the sklearn.metrics Python package.
681

682 **Graph plotting**

683 All bar graphs were plotted using GraphPad PRISM 8.0 software (GraphPad Software, Inc.,
684 CA, USA). Fig. 1b(i) and Fig. 5a were created using resources from BioRender.com. The sources
685 of images in Fig. 1 also included <https://www.rxhrx.ai/rxhrx2>, in addition to those listed in the
686 supplementary Table 1 & 2. Some microscopy images in the figures have been processed using
687 “Enhance Contrast...” from ImageJ⁶² for better presentation.
688

689 **Software and hardware**

690 The programming was conducted using Python v.3.7. Training and all evaluations were
691 performed on NVIDIA GeForce RTX 3090 GPUs. The deep learning framework of Microsnoop
692 used PyTorch⁶³ v.1.10.
693

694 **Data availability**

695 The links to download the raw data of training set and evaluation datasets are provided in
696 Supplementary Table 1-2. The new evaluation datasets generated by this study are available on
697 figshare:
698 https://figshare.com/articles/dataset/Microsnoop_a_generalist_tool_for_the_unbiased_representation_on_of_heterogeneous_microscopy_images/22197607.

700 SeqFISH+ mouse cortex dataset: Transcript data were downloaded from
701 <https://github.com/CaiGroup/seqFISH-PLUS>. Image data were provided by the authors of the
702 seqFISH+ paper.

703 All data in this study are available from the corresponding author upon reasonable request.
704

705 **Code availability**

706 Source code for Microsnoop, including detailed tutorial, is available on GitHub
707 (<https://github.com/cellimnet/microsnoop-publish>). A configured Amazon Machine Image (AMI)
708 will be made available upon publication for quickly and conveniently deploying Microsnoop for
709 microscopy image analysis.
710
711

712 **Acknowledgments**

713 We thank L. Cai at Caltech for providing seqFISH+ image data. We thank W.K. Wang and
714 L. Sun at Amazon Web Services China for their indispensable support in terms of computing
715 resources and technology. We are grateful for the support from ZJU PII-Molecular Devices Joint
716 Laboratory and support from "Medicine + X" interdisciplinary Center of Zhejiang University.
717 This study was supported by National Key R&D Program of China (2021YFC1712905), National
718 Natural Science Foundation of China (No. 82173941, No. 61872319), Key R&D Program of
719 Zhejiang Province (No. 2023C01039). Y.W. was supported by the Innovation Team and Talents
720 Cultivation Program of National Administration of Traditional Chinese Medicine (No.
721 ZYYCXTD-D-202002).
722

723 **Author contributions**

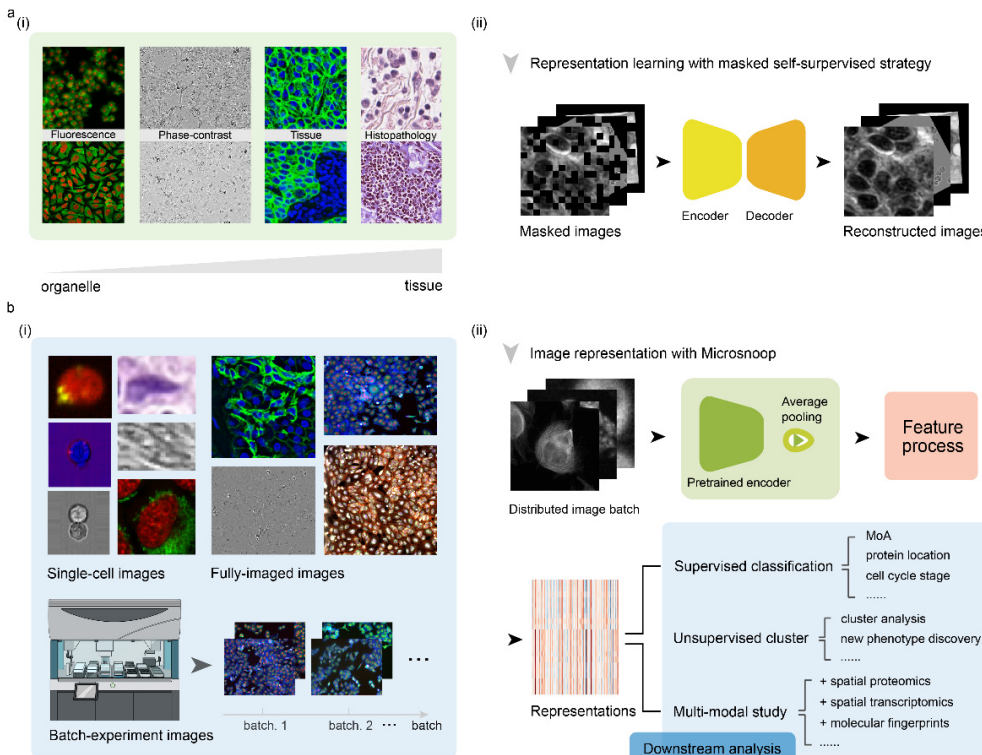
724 Y.W., X.C.Z. and R.W. supervised the study, D.J.X. acquired data, established pipeline,
725 conducted experiments and performed data analysis. D.J.X., Y.W., X.C.Z. and R.W. wrote the
726 manuscript.
727

728 **Competing interests**

729 The authors declare no competing interests.
730

731
732

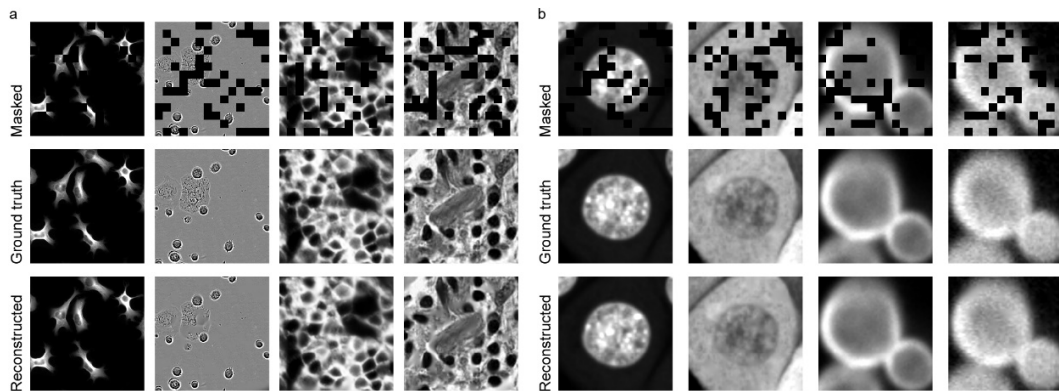
Figures and Tables



733
734
735
736
737
738
739
740
741
742
743
744
745
746
747
748
749

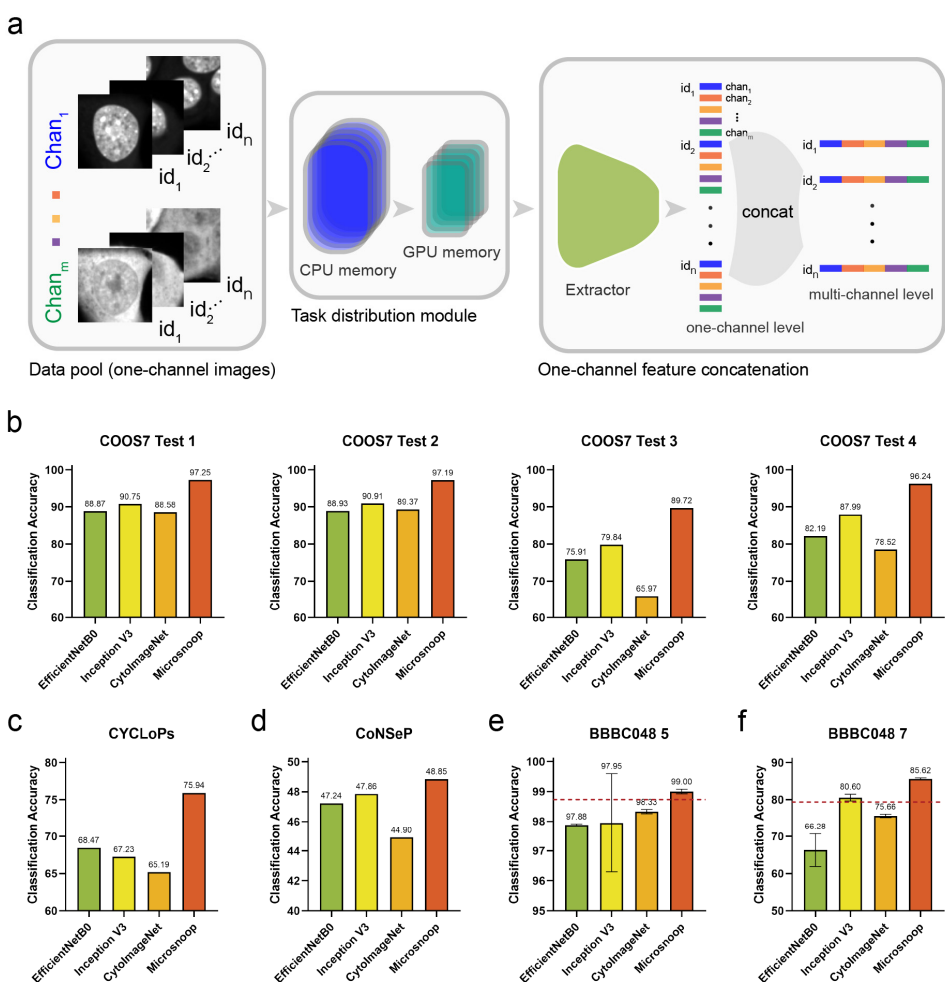
Fig. 1 | Design of Microsnoop for microscopy image representation. a, Schematic of the learning process. (i) Example of the four main category images are shown. The channels range from cellular organelles to tissues. (ii) A masked self-supervised learning strategy was employed and only images are required for training without additional manual annotation. One-channel masked images were set as the input and the Encoder-Decoder were required to reconstruct the original images. **b,** At test time, (i) Example images from various downstream tasks are shown, with different resolutions, number of channels and image types. These microscopy images are categorized into 3 types to ensure the broad coverage of image profiling needs. (ii) Application of Microsnoop. Firstly, images are managed by an in-built task distribution module (Fig. 3a), which generates one batch one-channel images for feature extraction. Each batch of images is fed into the pre-trained encoder, and the output smallest convolutional maps are processed by average pooling. Then, all extracted embeddings are processed according to different profiling tasks (introduced in the following section). The potential downstream analyses of our generalist representation tool are shown in the panel.

750



751
752 **Fig. 2 | Reconstruction results with Microsnoop.** **a**, Example results for images from the
753 validation set, with a masking ratio of 25% applied on inputs. One representative image is
754 selected for each image type. **b**, Example results for single-cell images from evaluated
755 data, with a masking ratio of 25% applied on inputs. The left two columns are from
756 COOS7 and the right two are from CYCLoPs. Two representative images (different
757 imaging channels of the same cell) are selected for each dataset. Example results on other
758 evaluated datasets are shown in Extended Data Figs. 4.
759

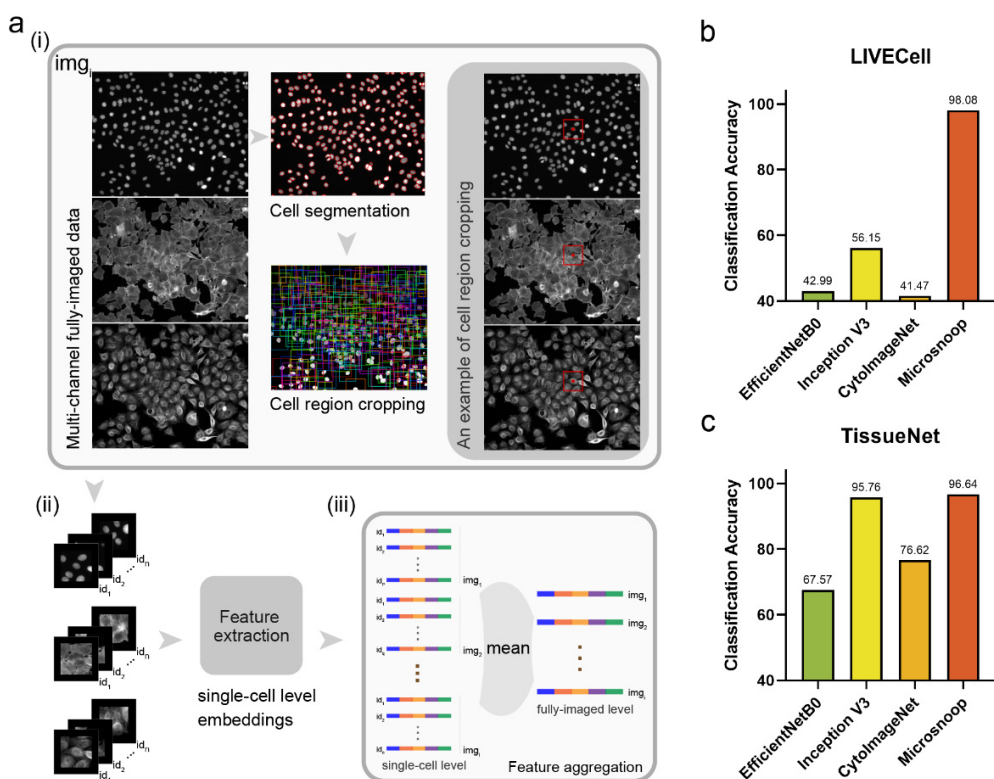
760



761
762
763
764
765
766
767
768
769
770
771

Fig. 3 | Profiling with Microsnoop on single-cell images. **a**, Pipeline. Every channel of the single-cell image is processed independently, and the one-channel level embeddings are concatenated to get multi-channel level image representations. A task distribution module is provided to prevent memory overflow. The Extractor denotes the pretrained encoder combined with the average pooling layer shown in Fig. 1a(ii). **b-f**, Benchmarks. **b**, Benchmark on COOS7, containing four separate test sets. **c**, Benchmark on CYCLOPs. **d**, Benchmark on CoNSeP. **e,f**, Benchmarks on BBBC048, with two different classification tasks. Performances reported by the original paper are shown with dotted red lines. Error bars represent the mean \pm SD of fivefold cross-validation results.

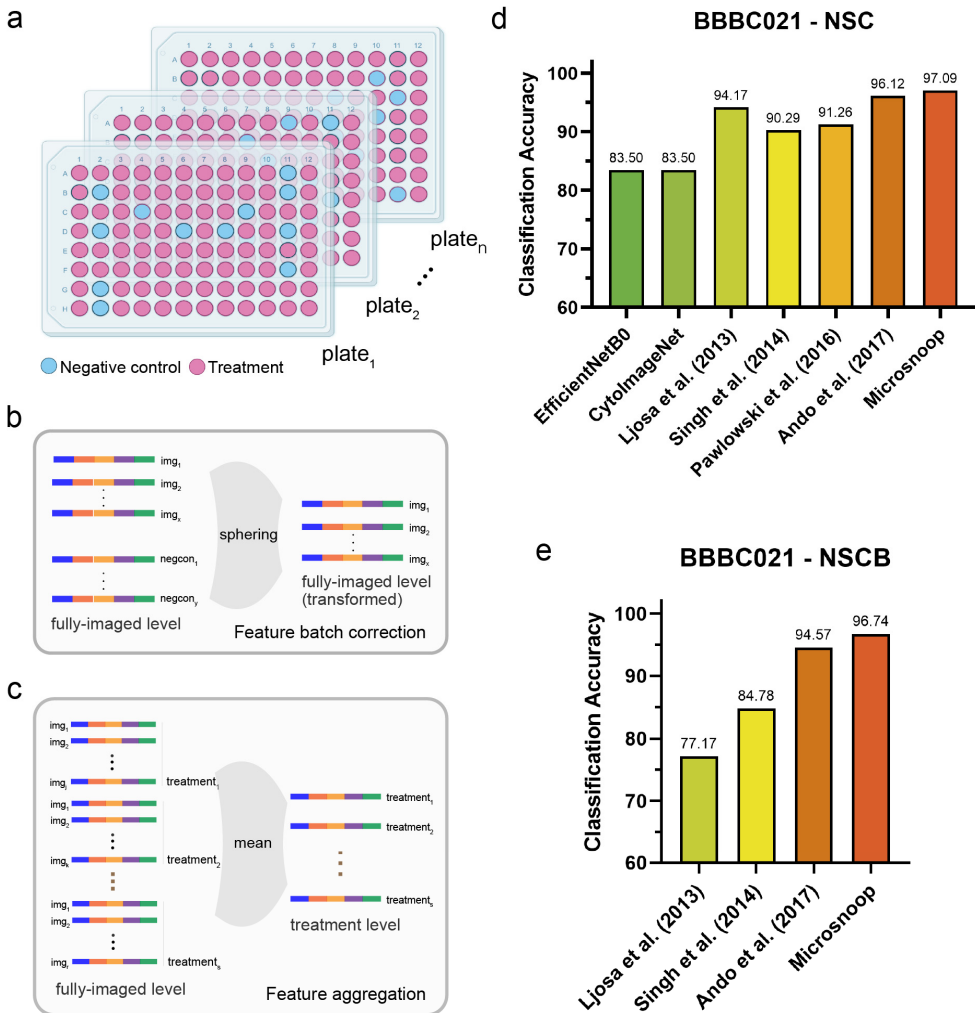
772



773
774
775
776
777
778
779
780

Fig. 4 | Profiling with Microsnoop on fully-imaged images. a, Pipeline. (i) Cell segmentation algorithm is conducted on the easiest channel (such as the nucleus channel) of the multi-channel fully-imaged image, then the cell region for each single cell is computed and cropped. (ii) Multi-channel single-cell images are processed as Fig. 3a, and (iii) the output single-cell level embeddings are aggregated to obtain the fully-imaged level image representations. **b, Benchmark on LIVECell.** **c, Benchmark on TissueNet.**

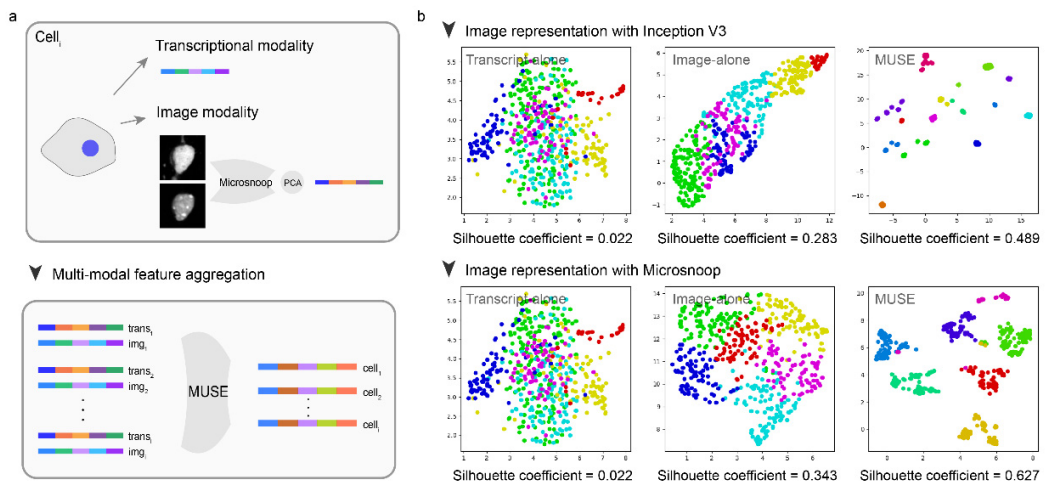
781



782
783
784
785
786
787
788
789

Fig. 5 | Profiling with Microsnoop on batch-experiment images. **a**, Schematic of multi-well plates in a drug screening experiment containing negative control wells and different treatment wells set in each plate. **b**, Batch correction on fully-imaged level representations. **c**, Feature aggregation on fully-imaged level embeddings to obtain treatment level image representations. **d,e**, Benchmark on BBBC021, with different evaluation metrics.

790

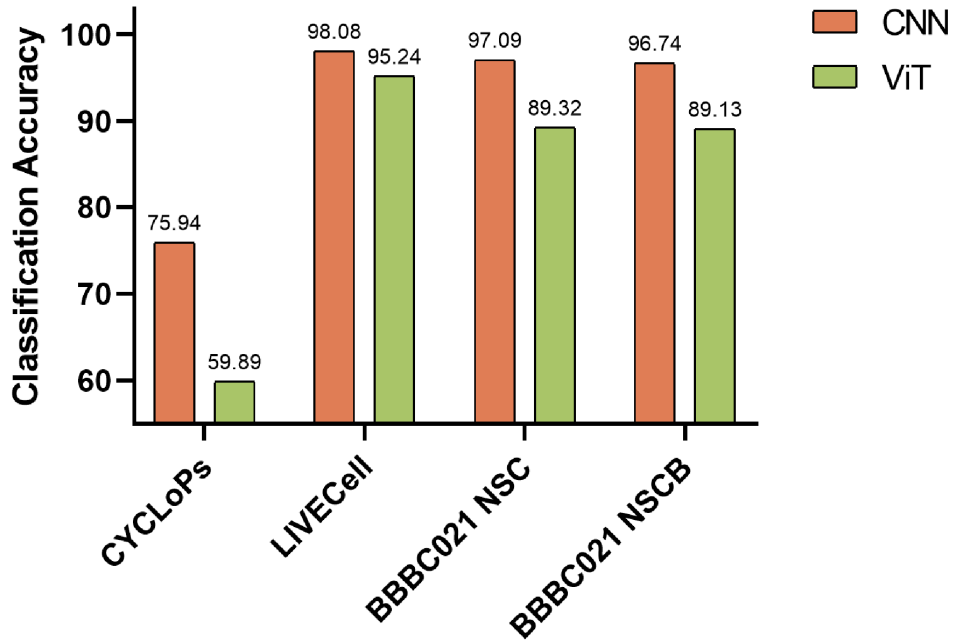


791
792
793
794
795
796
797
798

Fig. 6 | Joint use of Microsnoop and MUSE. **a**, Pipeline. Image modality data is first processed by Microsnoop, then PCA is performed on the output representations to reduce feature dimensionality. Finally, two modality representations are mixed by MUSE. **b**, UMAP visualization of different modality latent spaces on seqFISH+, using two different image representation methods. Silhouette score was used to quantify the separateness of clusters.

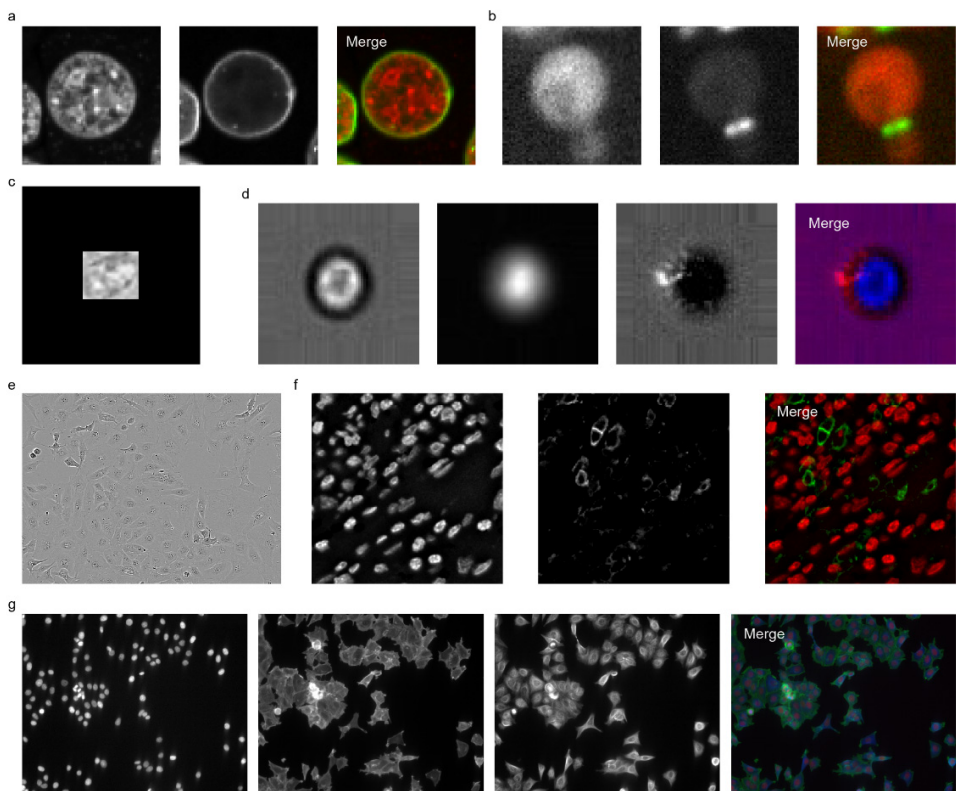
799 **Extended Data**

800
801



802
803 **Extended Data Fig. 1 | Performance evaluation of Microsnoop trained with different**
804 **network architectures.** Three representative datasets from seven evaluation datasets were
805 selected for the early trials: single-cell image task (CYCLOPs), fully-imaged image task
806 (LIVECell), and batch-experiment image task (BBBC021). The ViT architecture referred
807 to the MAE, and the classification accuracy for the corresponding dataset was reported.
808

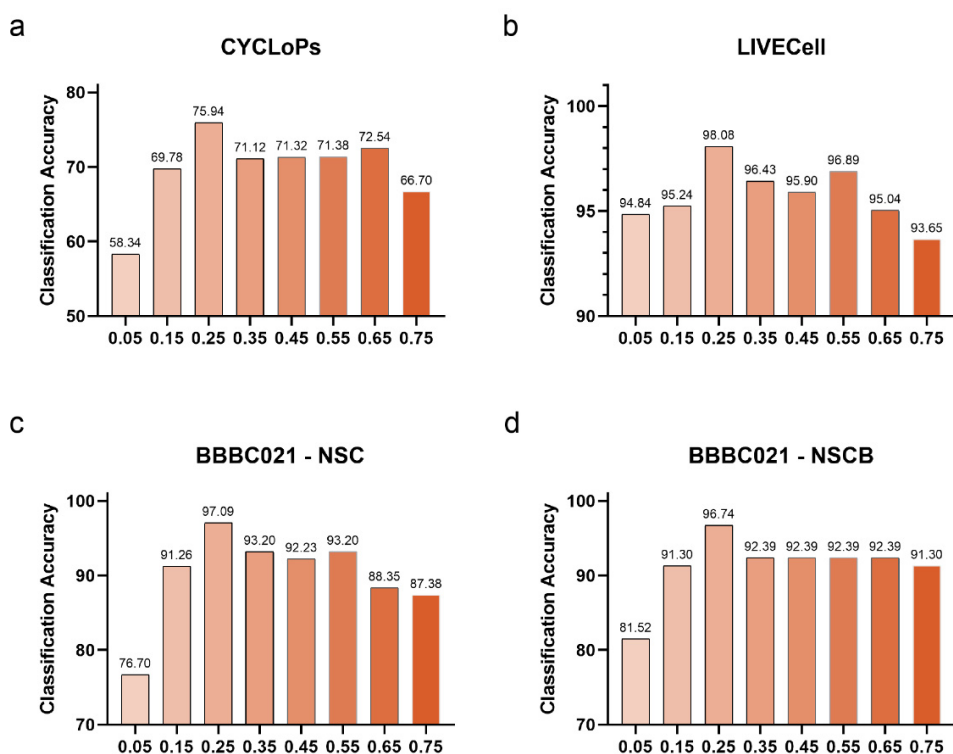
809



810
811
812
813
814

Extended Data Fig. 2 | Example images of evaluation datasets. Each channel of the example image was presented for each dataset: **a**, COOS7 **b**, CYCLOPs **c**, CoNSeP **d**, BBBC048 **e**, LIVECell **f**, TissueNet **g**, BBBC021.

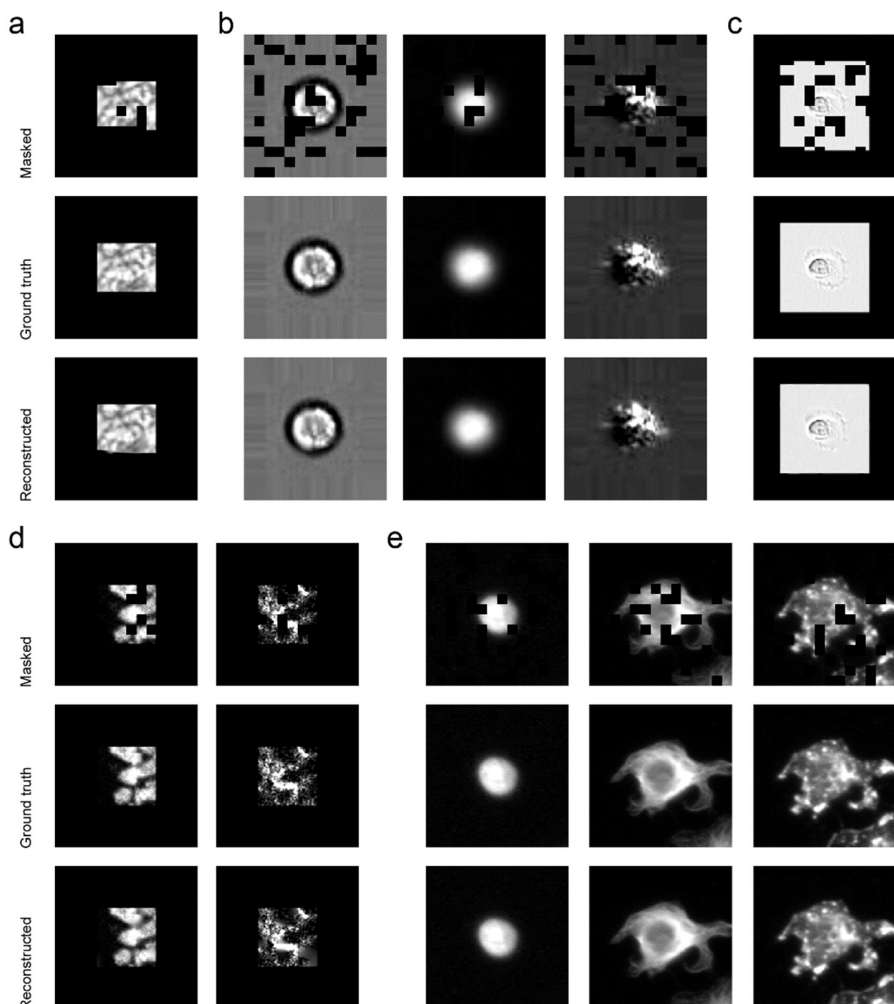
815



816
817
818
819
820
821
822

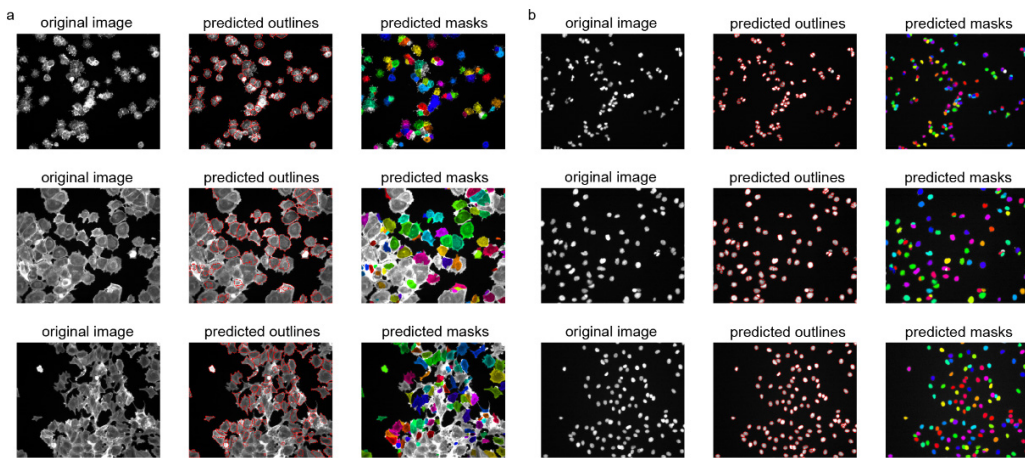
Extended Data Fig. 3 | Performance evaluation of Microsnoop trained with different mask ratios. Three representative datasets from seven evaluation datasets were selected for the early trials: **a**, Single-cell image task **b**, Fully-imaged image task **c,d**, Batch-experiment image task. The mask ratio was set ranging from 0.05 to 0.75, and the classification accuracy for the corresponding dataset was reported.

823



824
825 **Extended Data Fig. 4 | Reconstruction results with Microsnoop on the remaining**
826 **evaluation datasets.** Each channel of the example images from each dataset were
827 performed: **a**, CoNSeP **b**, BBBC048 **c**, LIVECell **d**, TissueNet **e**, BBBC021. For fully-
828 imaged image datasets (**c-e**), the processed single-cell images after cell region cropping
829 were used.
830

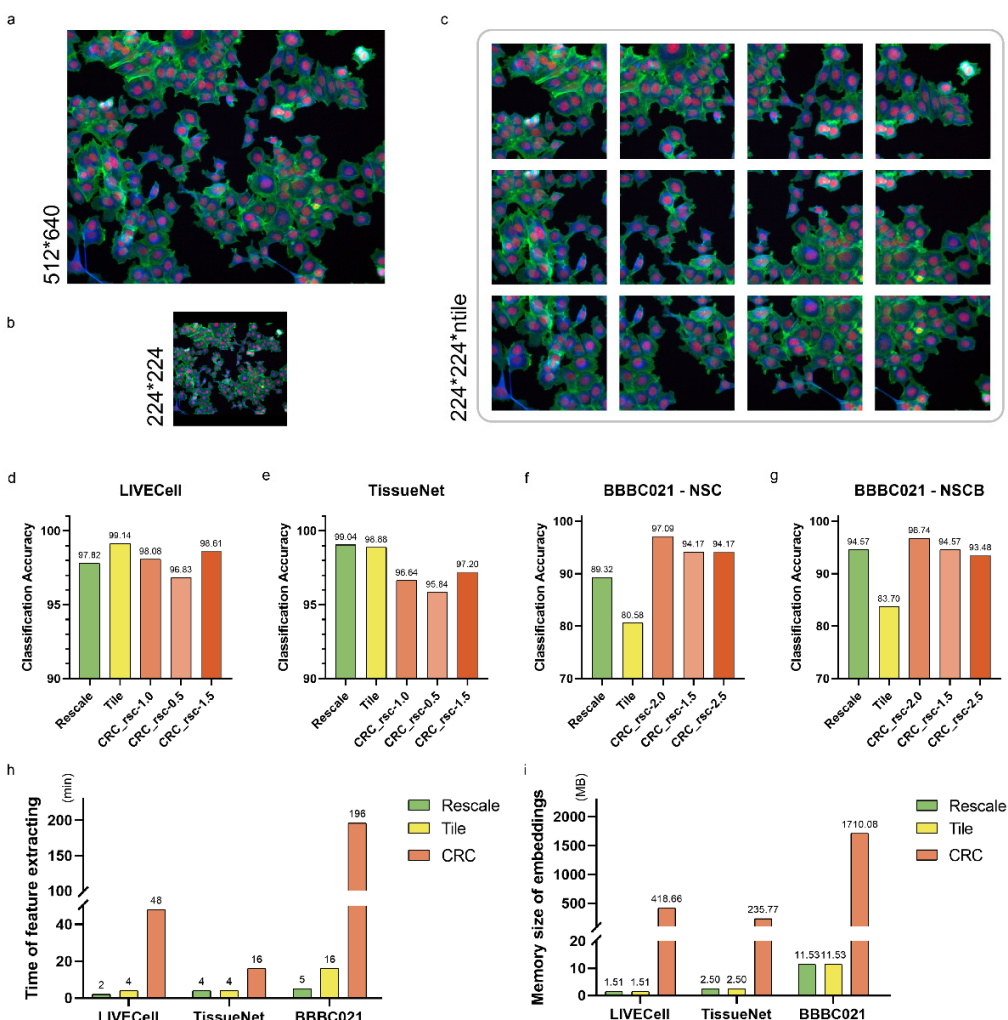
831



832

833 **Extended Data Fig. 5 | Example segmentation results of the generalist model for**
834 **high-content screening images.** Images were shown in pairs, with the original image on
835 the left and the segmentation results on the right using two visualization methods; the
836 predicted outlines show the boundary of each cell and the predicted masks mark the
837 segmented cells with different colors. Three images were selected from the BBBC021
838 dataset, in which cells were treated with different compounds and presented complex
839 phenotypes. Cell segmentation was conducted with Cellpose. **a**, Segmentation on F-actin
840 channel images. **b**, Segmentation on corresponding nucleus channel images.

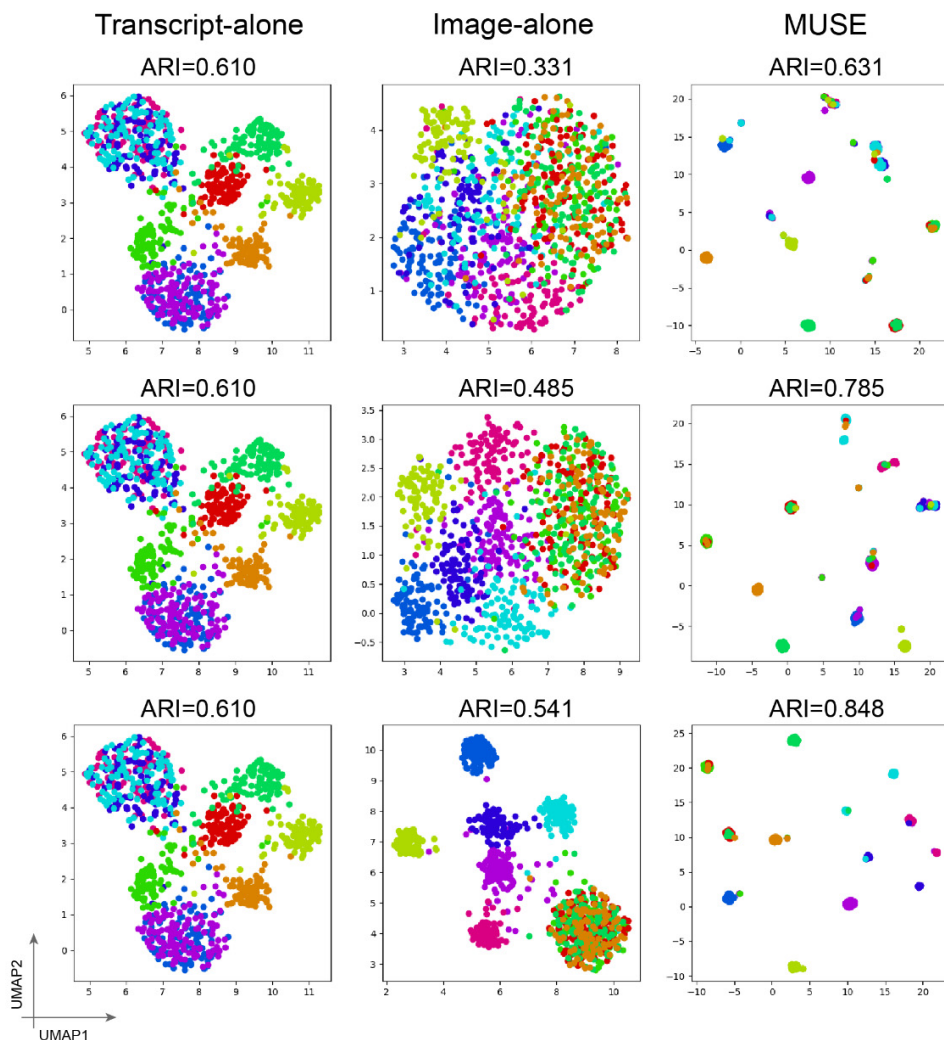
841



842
843
844
845
846
847
848
849
850
851
852
853

Extended Data Fig. 6 | Different profile modes of fully-imaged images. **a**, An example image. **b**, Example of the rescaling mode, where the original image was patched and rescaled to the input size (224*224). **c**, Example of the tile mode, where the original image is cropped to many 224*224 tiles (ntile) using the `make_tiles` function from the `cellpose.transforms` Python package, and the `tile_overlap` parameter was set as 0.1. **d-g**, Performance comparison of different modes on three evaluation datasets: **d**, LIVECell **e**, TissueNet **f,g**, BBBC021. The cell region cropping mode (CRC) was tested with different rescale constant to study the robustness. **h,i**, Time (**h**) and memory (**i**) cost of different modes. In the case of CRC mode, the memory cost computes the representations of all single-cell images, rather than the final fully-imaged level image representation.

854



855

856

Extended Data Fig. 7 | UMAP visualizations of latent embeddings from single- and combined-modality methods. Colors: ground truth subpopulation labels in simulation. Cluster accuracy is quantified using the adjusted Rand index (ARI).

857

858